



# Low-radiation dose scan protocol for preoperative imaging for dental implant surgery using deep learning-based reconstruction in multidetector CT

Yuki Sakai<sup>1</sup> · Erina Kitamoto<sup>2</sup> · Kazutoshi Okamura<sup>2</sup> · Shinya Takarabe<sup>1</sup> · Takashi Shirasaka<sup>1</sup> · Ryoji Mikayama<sup>1</sup> · Masatoshi Kondo<sup>1</sup> · Masato Tatsumi<sup>1</sup> · Tsukasa Kojima<sup>1</sup> · Toyoyuki Kato<sup>1</sup> · Kazunori Yoshiura<sup>2</sup>

Received: 7 November 2021 / Accepted: 13 December 2021

© The Author(s) under exclusive licence to Japanese Society for Oral and Maxillofacial Radiology 2021

## Abstract

**Objectives** This study aimed to investigate the impact of a deep learning-based reconstruction (DLR) technique on image quality and reduction of radiation exposure, and to propose a low-dose multidetector-row computed tomography (MDCT) scan protocol for preoperative imaging for dental implant surgery.

**Methods** The PB-1 phantom and a Catphan phantom 600 were scanned using volumetric scanning with a 320-row MDCT scanner. All scans were performed with a tube voltage of 120 kV, and the tube current varied from 120 to 60 to 40 to 30 mA. Images of the mandible were reconstructed using DLR. Additionally, images acquired with the 120-mA protocol were reconstructed using filtered back projection as a reference. Two observers independently graded the image quality of the mandible images using a 4-point scale (4, superior to reference; 1, unacceptable). The system performance function (SPF) was calculated to comprehensively evaluate image quality. The Wilcoxon signed-rank test was employed for statistical analysis, with statistical significance set at  $p$  value  $< 0.05$ .

**Results** There was no significant difference between the image quality acquired with the 40-mA tube current and reconstructed with the DLR technique (40DLR), and that acquired with the reference protocol (3.00, 3.00,  $p = 1.00$ ). The SPF at 1.0 cycles/mm acquired with 40DLR was improved by 156.7% compared to that acquired with the reference protocol.

**Conclusions** Our proposed protocol, which achieves a two-thirds reduction in radiation dose, can provide a minimally invasive MDCT scan of acceptable image quality for dental implant surgery.

**Keywords** Dental implant · MDCT · Radiation dose · Image quality · Deep learning

## Introduction

Dental implant surgery is a common procedure in clinical dental practice, and multidetector computed tomography (MDCT) and cone-beam computed tomography (CBCT) are the most common diagnostic imaging modalities used for preoperative dental implant planning [1–4]. These imaging modalities provide information on the height,

width, and angulation of the alveolar ridge, the quality of bone at the implant site, and the relationship between the implant site and adjacent structures, such as the mandibular canal. MDCT provides a superior contrast for soft tissues, whereas CBCT has a superior spatial resolution. Thus, CBCT is advantageous for the preoperative assessment of dental implant surgery. However, the use of CBCT is limited to patients who can remain stationary for a long time (approximately 10–25 s) in the sitting position during image acquisition [5, 6]. Therefore, MDCT, with its short irradiation time, could be an alternative for patients with involuntary movements. However, the radiation dose delivered by MDCT is generally higher than that delivered by CBCT [7]. Dentomaxillofacial scanning of the oral cavity, such as for the preoperative assessment of dental implant surgery, is conducted in the vicinity of radiosensitive organs, such as the thyroid gland and salivary glands; therefore, the

✉ Yuki Sakai  
yuki.sakai.san@gmail.com

<sup>1</sup> Division of Radiology, Department of Medical Technology, Kyushu University Hospital, 3-1-1, Maidashi, Higashi-ku, Fukuoka, Japan

<sup>2</sup> Department of Oral and Maxillofacial Radiology, Faculty of Dental Science, Kyushu University, Fukuoka, Japan

radiation dose should be minimized while maintaining diagnostic performance [8]. A previous study demonstrated that the combination of volumetric scanning and the iterative reconstruction (IR) technique achieved a 50% reduction in tube current while preserving image quality [9]. Volumetric scanning can acquire an entire dentomaxillofacial image within 1 s [10], and the IR technique lowers the radiation dose by reducing image noise [11].

In recent years, a deep learning-based reconstruction (DLR) technique has been introduced in clinical applications. This DLR technique reduces image noise while simultaneously increasing spatial resolution [12]. Previous reports have demonstrated that the DLR technique yielded better image quality for soft tissue and coronary CT angiography than the IR technique [12, 13]. However, the effect of the DLR technique on image quality for the dentomaxillofacial region (bone tissue) and the possibility of radiation dose reduction have not been investigated. Thus, there is a need to demonstrate the usefulness of the DLR technique in this region, where low radiation exposure is required. Therefore, this study aimed to investigate the impact of the DLR technique on image quality and reduction of radiation exposure to propose a low-dose MDCT scan protocol for dental implant surgery.

## Methods and materials

### Phantoms

A phantom of the mandibles of a human head (PB-1; Kyoto Kagaku, Kyoto, Japan; Fig. 1a) [14] was used for observer evaluation, and a Catphan phantom 600 (Phantom Laboratory, Greenwich, USA; Fig. 1b) [15] and a TOS phantom (Kyoto Kagaku, Kyoto, Japan; Fig. 1c) were used for physical characteristics analysis. The Catphan phantom (200 mm in diameter) contains two modules: a sensitometry module (CTP 404) and an image uniformity module (CTP 486).

### Image acquisition and reconstruction conditions

The phantoms were scanned with a 320-row MDCT scanner (Aquilion One Prism Edition; Canon Medical Systems, Otawara, Japan) using volumetric scanning. This scanning technique can acquire an entire dental image with a single rotation [10]. All scans were performed under the following conditions: tube voltage, 120 kV; tube rotation time, 0.5 s/rot.; and 0.5-mm collimation  $\times$  80 rows. The tube current was varied from 120 to 60 mA to 40 to 30 mA. Images were reconstructed with 1.0-mm thickness with an 80-mm field of view. In all acquisitions, the DLR (Advanced intelligent Clear-IQ Engine mild; Canon Medical Systems, Otawara, Japan) technique and IR (Adaptive Iterative Dose Reduction three-dimensional enhanced mild; Canon Medical Systems, Otawara, Japan) technique were performed with bone kernel. Hereafter, images acquired at a tube current of 120 mA and reconstructed using the DLR/IR technique are defined as 120DLR/120IR, and similarly for the other conditions. Additionally, images acquired by the 120-mA protocol were reconstructed using filtered back projection as a reference. Table 1 summarizes the details of the acquisition and reconstruction parameters.

### Qualitative assessment

For qualitative assessment, the mandible of the PB-1 phantom was scanned parallel to the occlusal plane. A dental radiologist and a radiological technologist with 9 and 8 years of experience, respectively, independently graded the image quality of the 54 mandible images (six images acquired by nine protocols) based on delineations of the alveolar bone and inferior dental canal. Figure 2 shows examples of six images used for visual evaluation. The 54 images were compared with the reference image using a 4-point scale (4, superior to reference; 3, comparable to reference; 2, acceptable but limited diagnostic

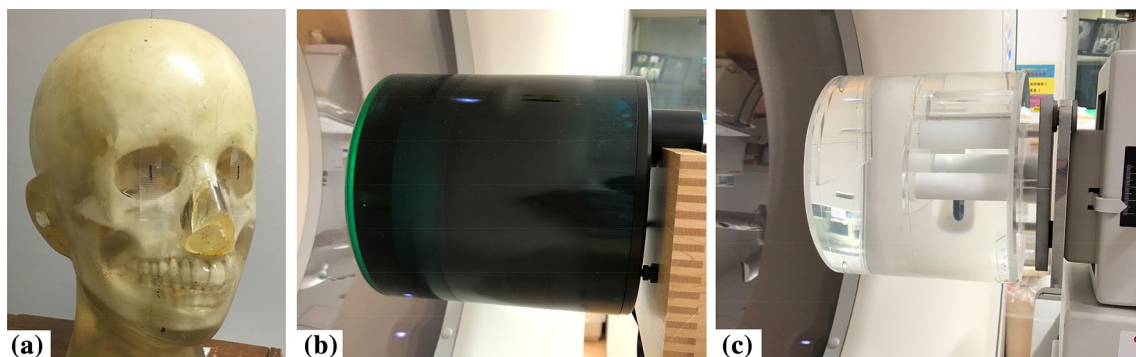


Fig. 1 Photos of **a** PB-1 phantom, **b** Catphan phantom, and **c** TOS phantom

**Table 1** Scan and reconstruction parameters

|                               |                           |
|-------------------------------|---------------------------|
| Scan method                   | Volumetric scanning       |
| Tube voltage (kVp)            | 120                       |
| Tube current (mA)             | 120, 60, 40, 30           |
| Rotation time (s/rotation)    | 0.5                       |
| Focal spot                    | Small                     |
| Collimation and detector rows | 0.5 mm × 80 rows          |
| Matrix size                   | 512 × 512                 |
| Slice thickness/interval (mm) | 1.0/1.0                   |
| Reconstruction method         | DLR, IR, FBP <sup>a</sup> |
| Reconstruction kernel         | Bone                      |
| FOV (mm)                      | 80                        |

*DLR* deep learning-based reconstruction, *IR* iterative reconstruction, *FBP* filtered back projection, *FOV* field of view

<sup>a</sup>FBP images acquired with a tube current of 120 mA were reconstructed as a reference

value; and 1, unacceptable). The images were randomized, and the observers were blinded to the acquisition and reconstruction conditions. Images were evaluated using a liquid-crystal display (RadiForce RX240, EIZO, Nanao, Ishikawa, Japan) with a preset window level of 500 HU and a window width of 3500 HU, and the reviewers were allowed to adjust the window set during evaluations. Reading time was not limited.

## Quantitative assessment

The spatial resolution, image noise, frequency characteristics of the image noise, and system performance function (SPF) were assessed in all acquisition and reconstruction parameters using CT measure version 098f (Japanese Society of CT Technology, Hiroshima, Japan) [16].

For spatial resolution assessment, in-plane and z-directional task-based modulation transfer function (TTF) curves were calculated using the CTP 404 module and TOS phantom. The in-plane TTF curves were calculated using an inserted disk-shaped object (Teflon, CT number at 120 kV, approximately 940 HU) surrounded by a square region of interest (ROI) according to the circular edge method [17]. The “Task” considered in this study was bone, and a Teflon insert was used to reproduce the bone contrast (approximately 840 HU). The z-directional TTF curves were calculated using the averaged sagittal image of the tilted rod object (Teflon) inserted in a TOS phantom surrounded by a square ROI, according to the slanted edge method [18]. The phantom was inclined at 3° to obtain sufficiently small data intervals during synthesis. One hundred CT slices were used for in-plane and z-directional TTF measurements to improve accuracy.

The standard deviation (SD) of the CT number was calculated as the assessment of image noise. A square ROI (256 × 256 pixels) was placed in the center of the CTP 486 image. The mean image noise was calculated from 50 CT slices for each protocol.

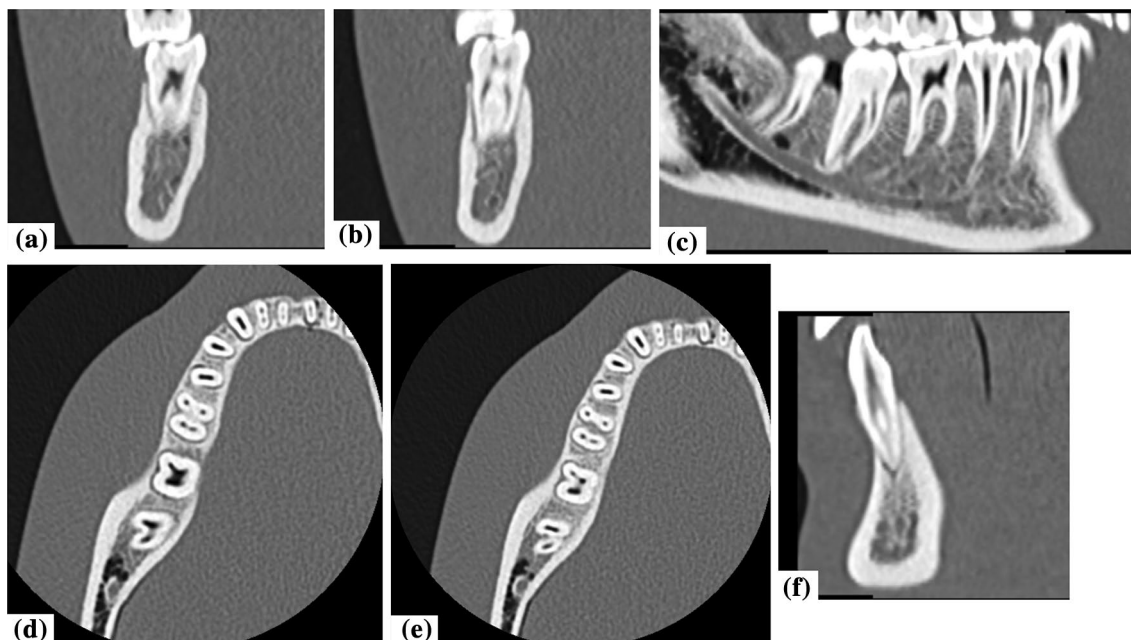


**Fig. 2** Example of images for the visual evaluation test: two buccolingual section images at the **a** first and **b** second molar, **c** a mesiodistal section image, two horizontal section images at the alveolar crest level (**d**, **e**), and **f** a sagittal section image at the mandibular central incisor

The noise power spectra (NPSs) were calculated to assess the frequency characteristics of the image noise. The radial frequency method was used for the NPS calculations [19]. The ROI size was set to  $256 \times 256$  pixels at the center of the CTP 486 image. The NPS curve for each protocol was acquired by averaging the NPS results from 100 CT slices.

The SPF was calculated as a function of spatial frequency for a comprehensive evaluation of image quality [18]. The SPF as a function of spatial frequency,  $u$ , is expressed as follows:

$$\text{SPF}^2(u) = \frac{\text{TTF}_{\text{in-plane}}^2(u)}{\text{NPS}(u)}. \quad (1)$$

The SPF [1] at 1.0 cycles/mm was compared in each protocol as an index of the comprehensive evaluation of image quality [9].

### Linear measurement

Two radiological technologists, each with 8 years of experience, independently measured 108 linear distances from 54 mandible images (width and height of each of the six images acquired by nine protocols). The bone width and height were measured as the alveolar crest distance and the vertical distance from the estimated alveolar crest to the upper wall of the mandibular canal, respectively (Fig. 3). When preparing the images for linear measurements, a CT scanner equipped with a position recording function was used to ensure the same position in the measured images acquired via all protocols. The images were randomized, and the operators were blinded to the acquisition and reconstruction conditions. The linear distance of each image was measured using a liquid-crystal display (RadiForce RX240, EIZO, Nanao, Ishikawa, Japan) with a preset window level of 500 HU and a window width of 3500 HU; the operators were allowed to adjust the window set during evaluations. The time for linear measurements was not limited.

### Radiation dose calculation

The volume CT dose index ( $\text{CTDI}_{\text{vol}}$ ) and dose length product (DLP) were recorded from the corresponding dose reports. The effective doses in each protocol were calculated by multiplying the DLP by the effective dose coefficients of  $0.0031 \text{ (mSv m Gy}^{-1} \text{ cm}^{-1})$  to estimate the head and neck region of adult patients [20].

### Statistical analysis

Data acquired by the visual evaluation test are reported as the mean  $\pm$  standard deviation (SD). Statistical analysis using the Wilcoxon signed-rank test was performed to compare the

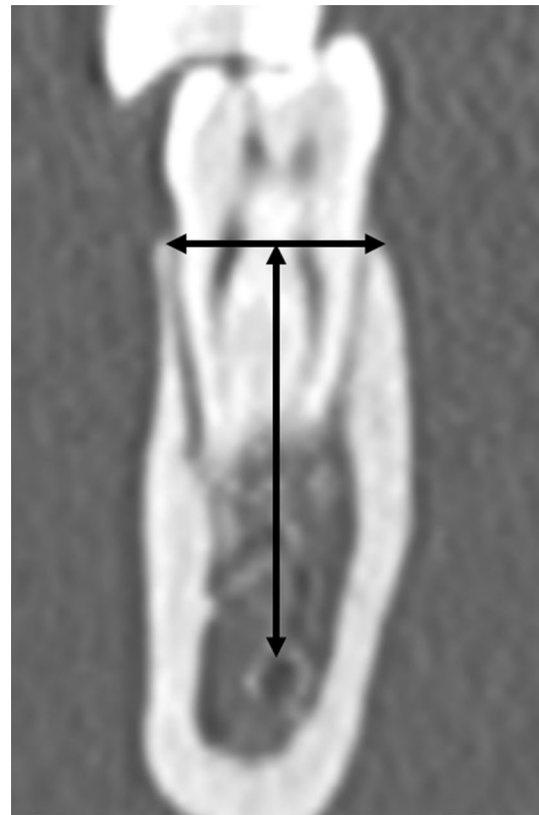


**Fig. 3** Example of buccolingual section images used for linear length measurement

image quality between each protocol and the reference protocol. Interobserver agreement was calculated using the kappa statistic ( $\leq 0.20$  = poor;  $0.21$ – $0.40$  = fair;  $0.41$ – $0.60$  = moderate;  $0.61$ – $0.80$  = substantial; and  $0.81$ – $1.00$  = almost perfect).

The mean and SD values of the differences between linear measurements obtained by each protocol and the reference protocol were recorded, and the differences between linear measurements obtained by each protocol and the reference protocol were analyzed using a one-sample  $t$  test. Thereafter, the reliability of the linear measurement between each protocol and the reference protocol was tested using the Bland–Altman analysis [21]. Inter- and intra-examiner agreements were evaluated using intraclass correlation coefficients (ICCs). The two linear measurements recorded by the first operator were used to calculate intra-examiner reliability. A time interval of 3 months was set to evaluate intra-examiner agreement. Statistical significance was set at  $p < 0.05$ . Statistical analysis was performed using JMP Pro 14.2.0 (SAS Institute, Cary, NC, USA).

### Ethical consideration

Our experimental phantom study did not require approval by an institutional review board.

## Results

### Qualitative evaluation

Table 2 shows the results of the observer evaluation test, and Fig. 4 shows the phantom images evaluated in the visual evaluation test. Observers gave higher scores to images acquired with a higher tube current for each reconstruction

method. The images reconstructed using the DLR technique were found to be superior to those reconstructed using the IR technique in the corresponding tube current setting. There was no significant difference between the image quality of 40DLR and that of the reference protocol ( $3.0 \pm 0.0$ ,  $3.0 \pm 0.0$ ,  $p = 1.00$ ); in contrast, the image quality of 40IR was significantly worse than that of the reference protocol ( $2.7 \pm 0.5$ ,  $3.0 \pm 0.0$ ,  $p = 0.036$ ). The two observers in our study showed moderate interobserver agreement ( $\kappa = 0.533$ ).

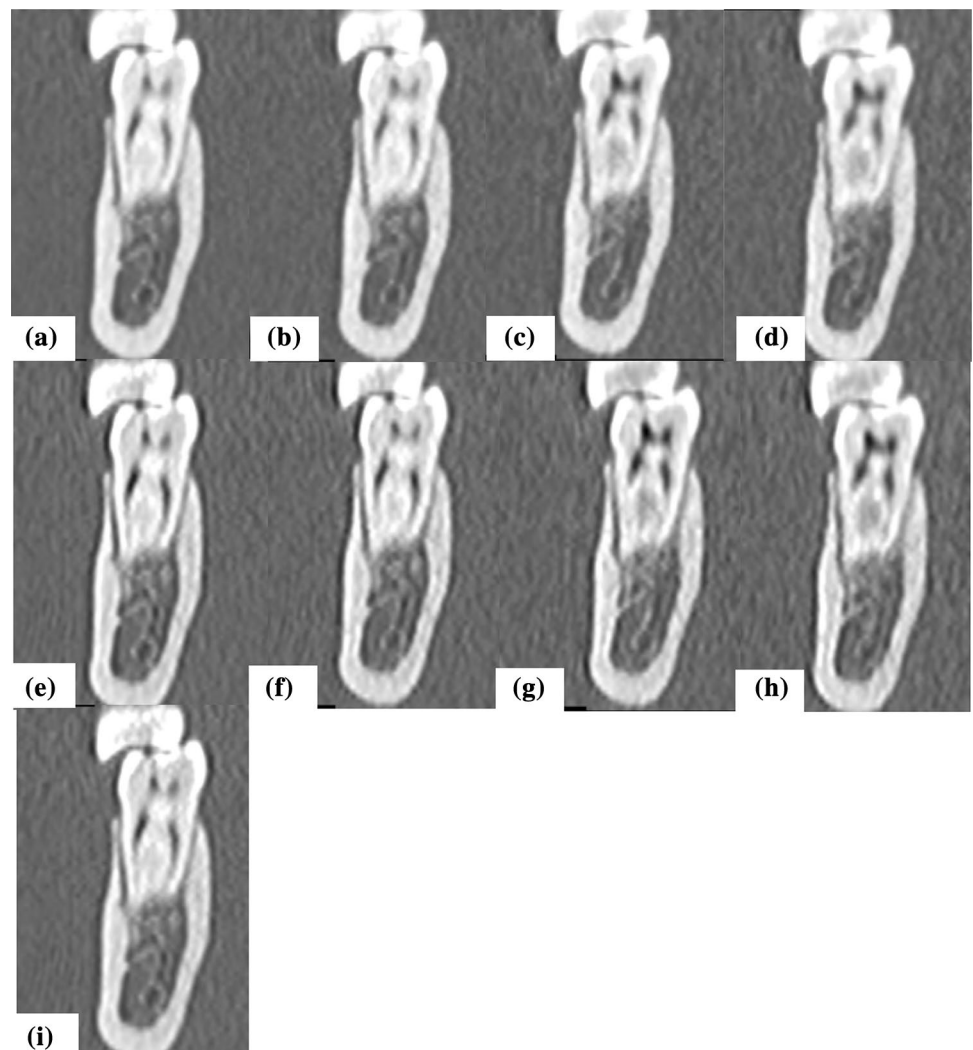
**Table 2** Image quality in each protocol as evaluated by two observers

| Protocol | Reconstruction method |                |               |                |                 |                |
|----------|-----------------------|----------------|---------------|----------------|-----------------|----------------|
|          | DLR                   | <i>p</i> value | IR            | <i>p</i> value | FBP (reference) | <i>p</i> value |
| 120 mA   | $3.3 \pm 0.5$         | 0.03           | $3.1 \pm 0.3$ | 0.32           | $3.0 \pm 0.0$   | 1.00           |
| 60 mA    | $3.1 \pm 0.3$         | 0.32           | $3.0 \pm 0.0$ | 1.00           | –               | –              |
| 40 mA    | $3.0 \pm 0.0$         | 1.00           | $2.7 \pm 0.5$ | 0.04           | –               | –              |
| 30 mA    | $2.9 \pm 0.2$         | 0.32           | $2.4 \pm 0.5$ | 0.002          | –               | –              |

Statistical analysis was conducted between each protocol and the reference protocol

*DLR* deep learning-based reconstruction, *IR* iterative reconstruction, *FBP* filtered back projection

**Fig. 4** Example of phantom images: deep learning-based reconstruction images acquired at a tube current of **a** 120, **b** 60, **c** 40, and **d** 30 mA and iterative reconstruction images acquired at a tube current of **e** 120, **f** 60, **g** 40, and **h** 30 mA, and **i** image acquired with the reference protocol

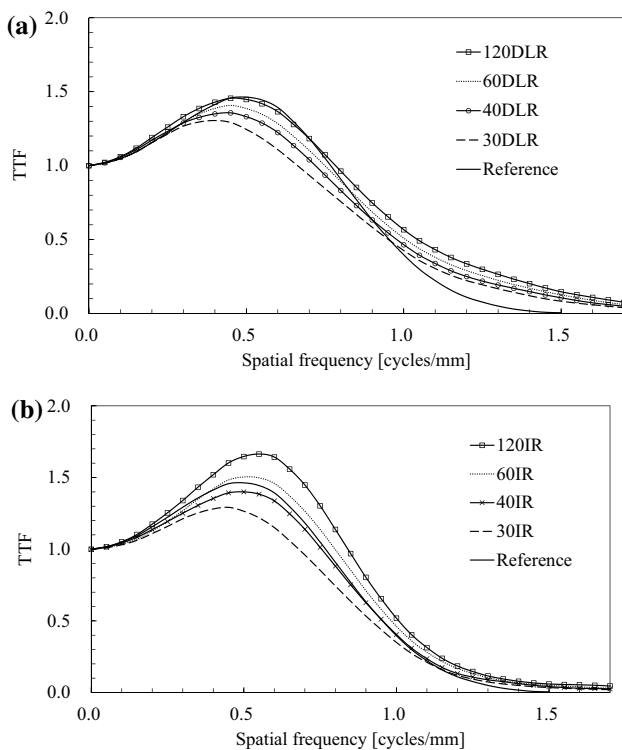


## Quantitative evaluation

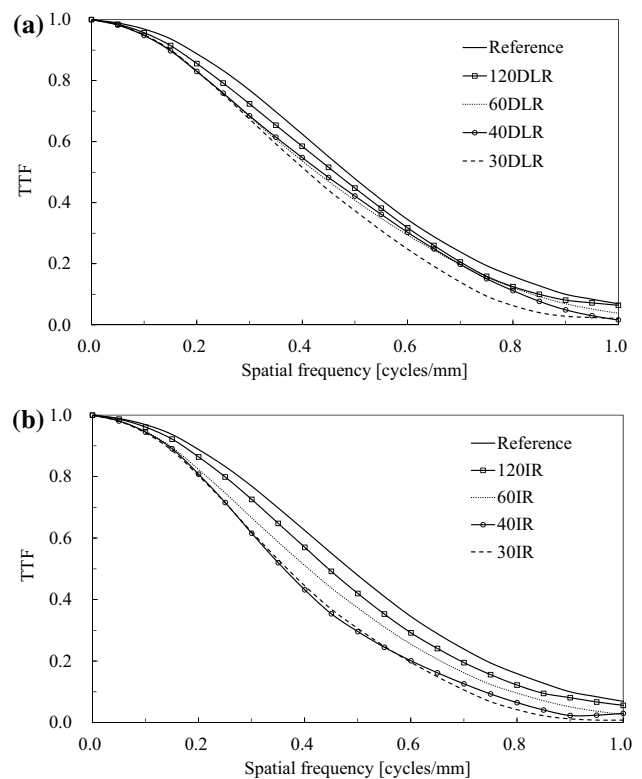
### Task transfer function

Figure 5a, b shows the comparisons of in-plane TTF measurements between the DLR protocols and reference protocol and between the IR protocols and reference protocol, respectively. The 10%TTF values of the 120-, 60-, 40-, and 30-mA protocols reconstructed with DLR/IR techniques and the reference protocol were 1.63/1.34, 1.57/1.31, 1.52/1.27, 1.45/1.24, and 1.22 cycles/mm, respectively. The shapes of the in-plane TTF curves reconstructed with DLR/IR indicated differences depending on the tube currents, and the 10%TTF values of the images reconstructed with DLR were higher than those of images reconstructed with IR at the corresponding tube current setting. Compared to 40IR, 40DLR provided a 19.3% higher spatial resolution at 10%TTF.

Figure 6a, b shows the comparisons of z-directional TTF measurements between DLR protocols and the reference protocol and between IR protocols and the reference protocol, respectively. The 10%TTF values of the 120-, 60-, 40-, and 30-mA protocols reconstructed with DLR/IR techniques and



**Fig. 5** Comparisons of in-plane TTF curves between **a** DLR and reference images and **b** IR and reference images. Each scan in 120DLR/IR, 60DLR/IR, 40DLR/IR, and 30DLR/IR was conducted with tube currents of 120, 60, 40, and 30 mA, respectively, and reconstructed with the DLR/IR algorithm. TTF, task-based modulation transfer function; DLR, deep learning-based reconstruction; IR, iterative reconstruction



**Fig. 6** Comparisons of z-directional TTF curves between **a** DLR and reference images and between **b** IR and reference images. Each scan in 120DLR/IR, 60DLR/IR, 40DLR/IR, and 30DLR/IR was conducted with tube currents of 120, 60, 40, and 30 mA, respectively, and reconstructed with the DLR/IR algorithm. TTF task-based modulation transfer function, DLR deep learning-based reconstruction, IR iterative reconstruction

the reference protocol were 0.85/0.84, 0.84/0.79, 0.82/0.74, 0.74/0.71, and 0.88 cycles/mm, respectively. The 10%TTF values of the images reconstructed with 120DLR and 120IR were slightly lower than those of the reference protocol.

### Image noise

The SD values of the 120-, 60-, 40-, and 30-mA protocols reconstructed with DLR/IR and the reference protocol were  $78.5 \pm 1.8/130.0 \pm 3.2$ ,  $104.6 \pm 3.4/160.6 \pm 3.2$ ,  $117.4 \pm 3.7/169.3 \pm 3.3$ ,  $122.2 \pm 3.4/169.6 \pm 2.8$ , and  $119.1 \pm 2.3$  HU, respectively. The image noise of the images reconstructed with DLR was dramatically decreased compared to that of images reconstructed with IR at the corresponding tube current setting.

### Noise power spectrum

Figure 7a, b shows the comparisons of the NPS curves between the DLR protocols and reference protocol and between the IR protocols and reference protocol,

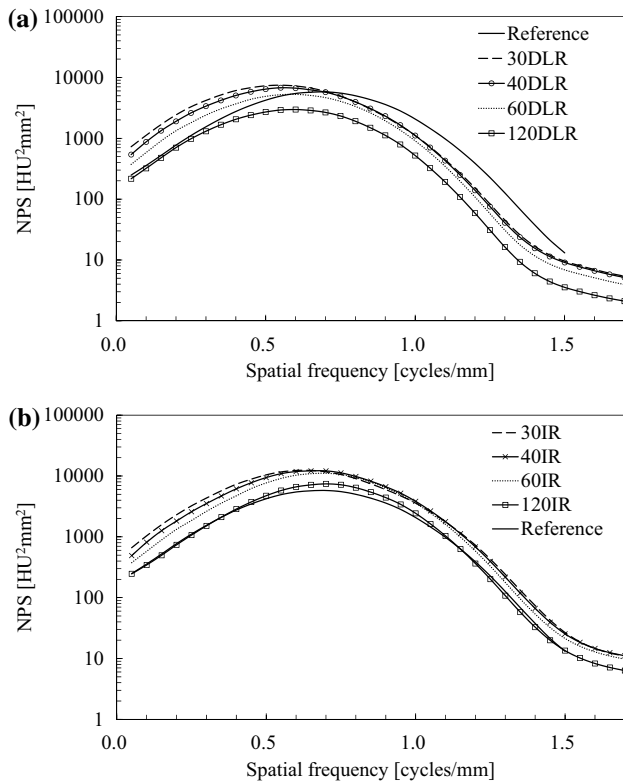


**Fig. 7** Comparisons of NPS curves between **a** DLR and reference images and **b** IR and reference images. Each scan in 120DLR/IR, 60DLR/IR, 40DLR/IR, and 30DLR/IR was conducted with tube currents of 120, 60, 40, and 30 mA, respectively, and reconstructed with the DLR/IR algorithm. *NPS* noise power spectrum, *DLR* deep learning-based reconstruction, *IR* iterative reconstruction

respectively. DLR significantly reduced noise power, especially at high frequencies, compared to IR. The relative noise power at 1.0 cycles/mm in 40DLR and 40IR compared to the reference protocol was 53.4% and 185.0%, respectively. The NPS curves reconstructed with DLR showed that the peaks of the NPS curves shifted to a low spatial frequency as the tube current decreased.

**System performance**

Figure 8a, b shows the comparisons of SPF curves between the DLR protocols and reference protocol and between the IR protocols and reference protocol, respectively. The SPF [1] at 1.0 cycles/mm acquired for each protocol is shown in Table 3. The SPF [1] at 1.0 cycles/mm acquired with 40DLR improved by 356.3% and 156.7% compared to that acquired with 40IR and the reference protocol, respectively, while the corresponding SPF [1] of 40IR worsened by 43.7% compared to that of the reference protocol.

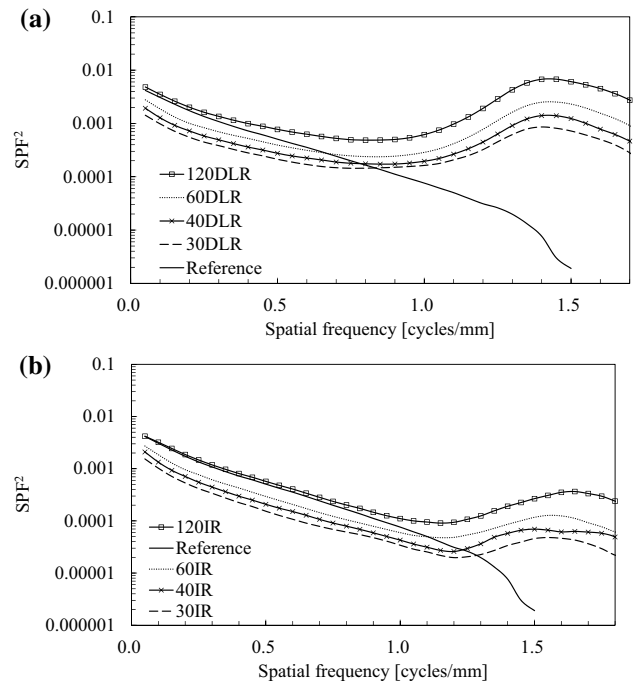


**Fig. 8** Comparisons of SPF curves between **a** DLR and reference images and **b** IR and reference images. Each scan in 120DLR/IR, 60DLR/IR, 40DLR/IR, and 30DLR/IR was conducted with tube currents of 120, 60, 40, and 30 mA, respectively, and reconstructed with the DLR/IR algorithm. *SPF* system performance function, *DLR* deep learning-based reconstruction, *IR* iterative reconstruction

**Linear measurement**

The differences between the linear measurements obtained by each protocol and the reference protocol are listed in Table 4. Supplementary Material Figs. 1 and 2 show the Bland–Altman plots between linear measurements obtained between the DLR protocols and reference protocol and between the IR protocols and reference protocol, respectively. There was a significant difference between the linear measurements obtained with the 30IR protocol and the reference protocol, while no significant differences were observed between the linear measurements obtained with

**Table 3** SPF<sup>2</sup> at 1.0 cycles/mm in each scanning and reconstruction method

| Protocol | Reconstruction method |         |                 |
|----------|-----------------------|---------|-----------------|
|          | DLR                   | IR      | FBP (reference) |
| 120 mA   | 0.00062               | 0.00011 | 0.00008         |
| 60 mA    | 0.00029               | 0.00006 | –               |
| 40 mA    | 0.00020               | 0.00004 | –               |
| 30 mA    | 0.00016               | 0.00003 | –               |

*SPF* system performance function, *DLR* deep learning-based reconstruction, *IR* iterative reconstruction, *FBP* filtered back projection

**Table 4** Differences between measurements obtained by each protocol and the reference protocol

| Protocol | Differences of measured value (mm) | 95% confidence interval limits (mm) |             | <i>p</i> value |
|----------|------------------------------------|-------------------------------------|-------------|----------------|
|          |                                    | Lower limit                         | Upper limit |                |
| 120DLR   | 0.057 ± 0.041                      | -0.028                              | 0.141       | 0.178          |
| 120IR    | 0.004 ± 0.030                      | -0.058                              | 0.066       | 0.900          |
| 60DLR    | 0.034 ± 0.044                      | -0.058                              | 0.126       | 0.451          |
| 60IR     | -0.010 ± 0.046                     | -0.106                              | 0.087       | 0.838          |
| 40DLR    | 0.051 ± 0.035                      | -0.022                              | 0.125       | 0.158          |
| 40IR     | -0.001 ± 0.039                     | -0.081                              | 0.081       | 0.995          |
| 30DLR    | -0.042 ± 0.042                     | -0.129                              | 0.045       | 0.326          |
| 30IR     | -0.121 ± 0.052                     | -0.229                              | -0.013      | 0.030          |

Each scan of 120DLR/IR, 60DLR/IR, 40DLR/IR, and 30DLR/IR protocols was acquired by volumetric scanning with tube currents of 120, 60, 40, and 30 mA, and reconstructed with DLR/IR algorithms, respectively

Data are given as mean ± standard deviation

Bland–Altman plots were performed between each protocol and the reference protocol, and statistical significance was set at *p* < 0.05

DLR deep learning-based reconstruction, IR iterative reconstruction

other protocols and the reference protocol. The ICCs for inter- and intra-observer agreement were 0.997 and 0.998, respectively.

### Radiation dose assessment

Table 5 shows the CTDI<sub>vol</sub>, DLP, and effective doses for each protocol. The effective dose of the 40-mA protocol was 31.3 μSv, which indicated a two-thirds reduction in the radiation exposure compared to the reference protocol.

### Discussion

This study proposed a low-radiation dose scanning protocol using the DLR algorithm that maintains diagnostic image quality in MDCT. This DLR technique achieved a two-thirds reduction in radiation dose. Our study demonstrated that the DLR technique also achieved low-dose imaging of the bone tissue. Furthermore, high-speed imaging with an irradiation time of 0.5 s can be employed in preoperative dental implant imaging in patients who cannot remain stationary.

According to the results of the visual evaluation test, there was no significant difference between the visual score of 40DLR and that of the reference protocol, while the visual score of 40IR was significantly inferior to that of the reference protocol. These results showed that the image quality acquired by the 40DLR was preserved, and the use of the DLR technique was recommended.

**Table 5** Comparison of radiation dose in each acquisition protocol

| Protocol | CTDI <sub>vol</sub> (mGy) | DLP (mGy cm) | Effective dose (μSv) |
|----------|---------------------------|--------------|----------------------|
| 120 mA   | 7.6                       | 30.3         | 93.9                 |
| 60 mA    | 3.8                       | 15.2         | 47.1                 |
| 40 mA    | 2.5                       | 10.1         | 31.3                 |
| 30 mA    | 1.9                       | 7.6          | 23.6                 |

CTDI<sub>vol</sub> volume computed tomography dose index, DLP dose length product

Based on the results of the quantitative assessment, the in-plane TTFs acquired with DLR were superior to those acquired with IR and the reference protocol, as the 10%TTF values of the DLR images were higher than those of IR images and the reference images. Moreover, the DLR technique effectively reduced the image noise, especially in the high-frequency range. The image noise of 40DLR was comparable to that of the reference protocol, although the image noise of 40IR was higher than that of the reference protocol. Higaki et al. previously demonstrated that the DLR algorithm improved spatial resolution and reduced image noise compared to the IR algorithm [13], and the results of this study support these findings. The performance evaluated by SPF indicated the superiority of the DLR, especially in the high-frequency range. Therefore, according to the results of qualitative and quantitative assessments, the image quality of 40DLR would be comparable to that obtained with the reference protocol.

The results of the linear measurement indicated that there was no significant difference between the linear measurements obtained with the 40DLR protocol and the reference protocol, although the reliability of the linear measurements obtained with 30IR was inferior to that obtained with the reference protocol. In a previous report by Al-Shawaf, the clinical significance of the absolute linear measurement differences was > 0.3 mm with a 95% confidence interval beyond ± 0.5 mm [1]. Therefore, the differences in 40DLR protocols used in this study were not clinically significant, and the use of 40DLR was reasonable in terms of image quality, linear measurement accuracy, and radiation dose.

The image qualities acquired by 40DLR and 60IR were comparable to those acquired by the reference protocol, and the effective doses of 40DLR and 60IR protocols were 31.1 and 47.1 μSv, respectively. Thus, compared to the IR technique, the DLR technique has the potential to further reduce the radiation dose by 16.9% relative to the reference protocol. Bornstein et al. reported that the effective dose of CBCT for a small FOV was 11–252 μSv [22]. Therefore, the effective dose of the 40DLR protocol was less than or equal to that of CBCT.

This study had several limitations. First, the image quality and linear measurement accuracy of the mandibular bone were evaluated using a phantom, and the linear measurement lacked a ground truth. Although our protocol can complete image acquisition in 0.5 s, we could not evaluate the difference in motion artifacts between MDCT and CBCT because a phantom image was evaluated in this study. Furthermore, the possibility of a reduction in radiation dose considering the presence of soft tissues could not be evaluated because the phantom used in this study was inappropriate for the evaluation of soft tissue. Therefore, it is necessary to confirm the extent to which the tube current is lowered during clinical examinations. Second, the applicability of the proposed protocol may be limited to specific cases wherein patients cannot remain stationary, since the spatial resolution of MDCT is inferior to that of CBCT. However, the effective dose of the 40DLR protocol was less than or equal to that of CBCT. Therefore, we believe that our proposed protocol is valuable as a way to scan patients who cannot remain stationary during imaging with minimal invasion. Third, the effect of the DLR algorithm on image qualities, such as spatial resolution and image noise, was not revealed. The detailed DLR algorithm was not disclosed to users, and the effect of this algorithm on the spatial resolution and image noise has complex variations depending on the acquisition and reconstruction conditions. However, under these experimental conditions, the DLR algorithm comprehensively improved the image quality and reduced the radiation dose. Fourth, this study demonstrated the results of reconstruction algorithms developed by a single manufacturer. Further studies are needed to investigate the quality of images reconstructed using other DLR algorithms developed by other manufacturers.

## Conclusion

We propose a low-dose scan protocol using the DLR technique in MDCT that achieves a two-thirds reduction in the radiation dose while preserving image quality. This high-speed scanning protocol can provide a minimally invasive CT scan for dental implant surgery.

**Supplementary Information** The online version contains supplementary material available at <https://doi.org/10.1007/s11282-021-00584-w>.

**Author contributions** YS contributed to conceptualization, investigation, writing and revising the draft critically for important intellectual content, final approval of the version to be published, and agreement to be accountable for all aspects of the work. EK co-author contributed to conceptualization, interpretation of data for the work, writing and revising the draft critically for important intellectual content, and agreement to be accountable for all aspects of the work. KO co-author was involved in methodology, interpretation of data for the work, revising the draft critically for important intellectual content, and agreement to

be accountable for all aspects of the work. ST co-author was involved in methodology, formal analysis, revising the draft critically for important intellectual content, and agreement to be accountable for all aspects of the work. TS co-author contributed to methodology, formal analysis, revising the draft critically for important intellectual content, final approval of the version to be published, and agreement to be accountable for all aspects of the work. RM and MK co-authors were involved in investigation, revising the draft critically for important intellectual content, final approval of the version to be published, and agreement to be accountable for all aspects of the work. MT and TK co-authors were involved in revising the draft critically for important intellectual content, final approval of the version to be published, and agreement to be accountable for all aspects of the work. KY supervisor contributed to conceptualization, revising the draft critically for important intellectual content, final approval of the version to be published, and agreement to be accountable for all aspects of the work.

**Funding** This research did not receive any specific grant from funding agencies in the public, commercial, or not-for-profit sectors.

## Declarations

**Conflict of interest** The authors declare that they have no conflict of interest.

**Ethical approval** Not applicable (this article does not contain any studies with human or animal subjects performed by the any of the authors).

**Informed consent** Not applicable.

## References

1. Al-Ekrish AA, Al-Shawaf R, Alfaleh W, Hörmann R, Puelacher W, Widmann G. Comparability of dental implant site ridge measurements using ultra-low-dose multidetector row computed tomography combined with filtered back-projection, adaptive statistical iterative reconstruction, and model-based iterative reconstruction. *Oral Radiol.* 2019;35:280–6.
2. Al-Ekrish AA, Al-Shawaf R, Schullian P, Al-Sadhan R, Hörmann R, Widmann G. Validity of linear measurements of the jaws using ultralow-dose MDCT and the iterative techniques of ASIR and MBIR. *Int J Comput Assist Radiol Surg.* 2016;11:1791–801.
3. Hsu JT, Huang HL, Fuh LJ, Li RW, Wu J, Tsai MT, et al. Location of the mandibular canal and thickness of the occlusal cortical bone at dental implant sites in the lower second premolar and first molar. *Comput Math Methods Med.* 2013;2013: 608570.
4. Naitoh M, Nakahara K, Suenaga Y, Gotoh K, Kondo S, Arijji E. Comparison between cone-beam and multislice computed tomography depicting mandibular neurovascular canal structures. *Oral Surg Oral Med Oral Pathol Oral Radiol Endod.* 2010;109:e25–31.
5. Veldhoen S, Schöllchen M, Hanken H, Precht C, Henes FO, Schön G, et al. Performance of cone-beam computed tomography and multidetector computed tomography in diagnostic imaging of the midface: a comparative study on Phantom and cadaver head scans. *Eur Radiol.* 2017;27:790–800.
6. Abdelkarim A. Myths and facts of cone beam computed tomography in orthodontics. *J World Fed Orthod.* 2012;1:e3–8.
7. Miracle AC, Mukherji SK. Conebeam CT of the head and neck, part I: physical principles. *AJNR Am J Neuroradiol.* 2009;30:1088–95.

8. Brenner DJ, Elliston CD, Hall EJ, Berdon WE. Estimated risks of radiation-induced fatal cancer from pediatric CT. *AJR Am J Roentgenol.* 2001;176:289–96.
9. Sakai Y, Okamura K, Kitamoto E, Kami YN, Shirasaka T, Mikayama R, et al. Improved scan method for dental imaging using multidetector computed tomography: a phantom study. *Dentomaxillofac Radiol.* 2020;49:20190462.
10. Lin WC, Wang HH, Hsu WL, Cao BH, Chen DJ, Tsai CJ. Investigation of an optimized scanning protocol for the dentomaxillofacial region using 320-slice multidetector computed tomography. *Dentomaxillofac Radiol.* 2017;46:20160395.
11. Nagatani Y, Takahashi M, Murata K, Ikeda M, Yamashiro T, Miyara T, et al. Lung nodule detection performance in five observers on computed tomography (CT) with adaptive iterative dose reduction using three-dimensional processing (AIDR 3D) in a Japanese multicenter study: comparison between ultra-low-dose CT and low-dose CT by receiver-operating characteristic analysis. *Eur J Radiol.* 2015;84:1401–12.
12. Tatsugami F, Higaki T, Nakamura Y, Yu Z, Zhou J, Lu Y, et al. Deep learning-based image restoration algorithm for coronary CT angiography. *Eur Radiol.* 2019;29:5322–9.
13. Higaki T, Nakamura Y, Zhou J, Yu Z, Nemoto T, Tatsugami F, et al. Deep learning reconstruction at CT: phantom study of the image characteristics. *Acad Radiol.* 2020;27:82–7.
14. Watanabe H, Honda E, Tetsumura A, Kurabayashi T. A comparative study for spatial resolution and subjective image characteristics of a multi-slice CT and a cone-beam CT for dental use. *Eur J Radiol.* 2011;77:397–402.
15. Davis AT, Palmer AL, Pani S, Nisbet A. Assessment of the variation in CT scanner performance (image quality and Hounsfield units) with scan parameters, for image optimisation in radiotherapy treatment planning. *Phys Med.* 2018;45:59–64.
16. Ichikawa K. CTmeasure; 2012–2014. Retrieved from: <http://www.jsct-tech.org/>. Hiroshima: Japanese Society of CT Technology.
17. Richard S, Husarik DB, Yadava G, Murphy SN, Samei E. Towards task-based assessment of CT performance: system and object MTF across different reconstruction algorithms. *Med Phys.* 2012;39:4115–22.
18. Ichikawa K, Kawashima H, Shimada M, Adachi T, Takata T. A three-dimensional cross-directional bilateral filter for edge-preserving noise reduction of low-dose computed tomography images. *Comput Biol Med.* 2019;111: 103353.
19. Ghetti C, Ortenzia O, Serreli G. CT iterative reconstruction in image space: a phantom study. *Phys Med.* 2012;28:161–5.
20. Valentin J, International Commission on Radiation Protection. Managing patient dose in multi-detector computed tomography (MDCT). ICRP Publication 102. *Ann ICRP.* 2007;37:1–79.
21. Bland JM, Altman DG. Statistical methods for assessing agreement between two methods of clinical measurement. *Lancet.* 1986;1:307–10.
22. Bornstein MM, Scarfe WC, Vaughn VM, Jacobs R. Cone beam computed tomography in implant dentistry: a systematic review focusing on guidelines, indications, and radiation dose risks. *Int J Oral Maxillofac Implants.* 2014;29(Suppl):55–77.

**Publisher's Note** Springer Nature remains neutral with regard to jurisdictional claims in published maps and institutional affiliations.